Computer Physics Communications 69 (1992) 287–298
North-Holland

Computer Physics Communications

Axisymmetric MHD equilibrium solver with bicubic Hermite elements

H. Lütjens, A. Bondeson and A. Roy

Centre de Recherches en Physique des Plasmas, Association Euratom – Confédération Suisse, Ecole Polytechnique Fédérale de Lausanne, 21, av. des Bains, CH-1007 Lausanne, Switzerland

Received 21 May 1990; in final form 10 July 1991

A numerical code using Hermite bicubic finite elements has been developed for the computation of axisymmetric magnetohydrodynamic (MHD) equilibria. The code provides a mapping to flux coordinates for MHD stability calculations. Several test cases are studied to show the convergence rate for the equilibrium. Convergence tests are also presented for the eigenvalues of the stability calculations when the equilibrium mesh is varied.

1. Introduction

For the study of magnetohydrodynamic (MHD) stability, accurate, flexible and efficient computation of equilibrium solutions is essential. Several numerical codes have been developed for this purpose. These codes use various numerical techniques such as conforming [1] or non-conforming [2] linear finite elements, finite differences [3–5], spectral decomposition [6], or a variational moment method [7,8]. In the present paper, we document a recently developed code using bicubic Hermite elements. It will be shown by comparison to codes using linear elements and second-order accurate finite differences, that the improved convergence properties of the bicubic elements give considerable savings in computation time for typical tokamak applications. Such comparisons are made for the convergence of the equilibrium itself and in addition for that of the eigenvalues computed by MHD stability codes when the equilibrium mesh is refined and the stability mesh is held fixed. To our knowledge, this is the first time that such convergence tests of the MHD growth rates are presented in the literature. Nevertheless, this appears to be the most direct way to measure the performance of an equilibrium code for MHD stability studies.

We have named the equilibrium code CHEASE (**C**ubic **H**ermite **E**lement **A**xisymmetric **S**tatic MHD **E**quilibrium solver). It solves the Grad–Shafranov equation with a prescribed, but rather arbitrarly shaped, plasma boundary and provides input for two MHD stability codes, ERATO [9] and MARS [10].

2. Formulation of the equilibrium problem

The problem of axisymmetric MHD equilibrium is well known [11]. The magnetic field can be represented as

$$\boldsymbol{B} = T\nabla\phi + \nabla\phi \times \nabla\Psi, \tag{1}$$

where ϕ is the ignorable toroidal angle (see fig. 1) and Ψ is the poloidal magnetic flux function. In the case of static MHD equilibrium, the poloidal current flux function T and the isotropic plasma pressure p are functions of Ψ. The equilibrium condition is given by the Grad–Shafranov equation [12–14]

$$\nabla \cdot \frac{1}{r^2}\nabla\Psi = -\frac{\mathrm{d}p}{\mathrm{d}\Psi} - \frac{1}{2r^2}\frac{\mathrm{d}T^2}{\mathrm{d}\Psi} = \frac{j_\phi}{r}, \tag{2}$$

where j_ϕ denotes the toroidal plasma current density.

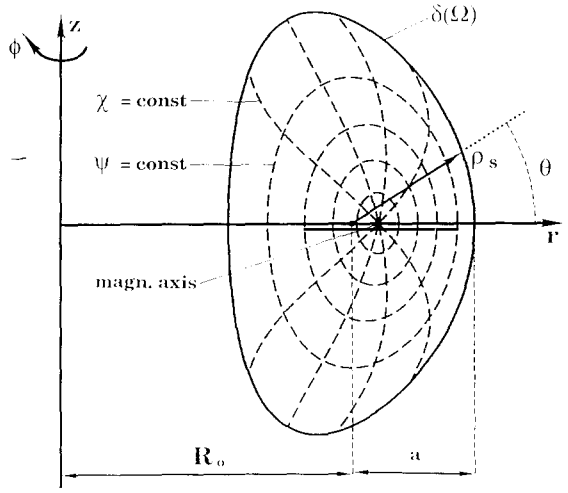

Fig. 1. The cylindrical coordinates (r, z, ϕ) in toroidal geometry.

CHEASE solves eq. (2) over the plasma cross-section Ω with the fixed boundary condition $\Psi \equiv 0$ on $\delta\Omega$ using bicubic Hermite elements for Ψ. In the following, we consider cases in which Ψ is negative everywhere inside the plasma and the total plasma current

$$I = \int_{\Omega} j_{\phi} \, \mathrm{d}S \tag{3}$$

is positive.

For the solution of equilibrium equation (2), the plasma cross-section Ω is transformed into a rectangular region $0 \le \sigma \le 1$, $0 \le \theta \le 2\pi$ by the use of a modified and non-orthogonal coordinate system (σ, θ) related to the cylindrical coordinates (r, z) by

$$\begin{aligned} r &= \sigma\rho_s(\theta) \cos\theta + r_0, \\ z &= \sigma\rho_s(\theta) \sin\theta + z_0 \end{aligned} \tag{4}$$

(see fig. 1). Details concerning the solution of the Grad–Shafranov equation are given in appendix A. In appendix B we show how a single solution of the Grad–Shafranov equation may be used to generate a whole family of equilibria with fixed poloidal beta and internal inductance, but with different plasma currents or safety factors.

3. Convergence of the equilibrium

In this section, we show the convergence of the equilibrium solution with respect to the cell size. For these tests, we use an equal number of intervals in the σ- and θ-directions, $N_\sigma = N_\theta = N$, and the "cell size" is defined as $h = 1/N$. Standard error estimates [15] predict that Ψ itself converges with an $\mathcal{O}(h^4)$ error, while the error in $\nabla\Psi$ is $\mathcal{O}(h^3)$.

Here, we use two different quantities to record the convergence, namely, the poloidal magnetic field energy

$$\mathscr{W}_B = \tfrac{1}{2}\int_{\sigma=0}^{1}\int_{\theta=0}^{2\pi} \sigma\rho_s^2(\theta)\frac{|\nabla\Psi|^2}{r}\mathrm{d}\sigma \, \mathrm{d}\theta, \tag{5}$$

and the position of the magnetic axis. In the special case where the equilibrium equation (2) is linear, i.e. j_ϕ is independent of Ψ, the poloidal magnetic field energy is expected to converge as $\mathcal{O}(h^6)$ [15]. For an up–down symmetric equilibrium, the magnetic axis where $\nabla\Psi = 0$ will occur at $(r, z) = (R_m, 0)$. Evidently, R_m should have the same convergence properties as $\partial\Psi/\partial r$, i.e. the error should be $\mathcal{O}(h^3)$. We point out that CHEASE can also deal with equilibria which are up–down asymmetric.

In all convergence tests to follow, we have used a packing of the θ-mesh in such a way that the area of all cells in the θ-direction (for fixed σ) is the same. Two different classes of equilibria will be considered: analytic Solovev equilibria [16] and non-linear equilibria where p and T^2 are low-order polynomials in $\Psi/\Psi_{\min}$.

3.1. Solovev equilibrium

A standard test case for any equilibrium code is the family of analytic equilibria found by Solovev [16] for which eq. (2) is a linear equation for Ψ. We consider the following special cases, where

$$\begin{aligned} p(\Psi) &= -\frac{1+E^2}{ER_0^3 q_0}\Psi, \\ T(\Psi) &= T_0 = 1, \end{aligned} \tag{6}$$

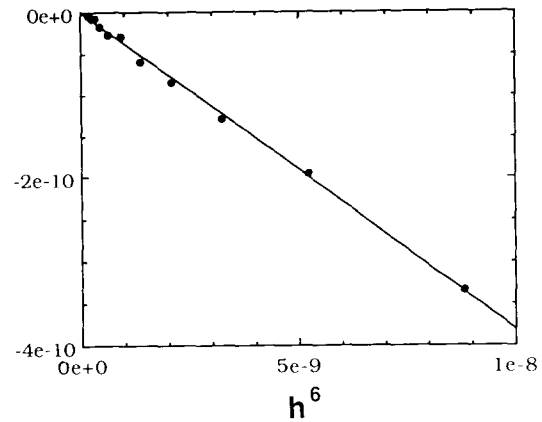

Fig. 2. Convergence of the poloidal magnetic energy of the Solovev test case. The regression curve is $\mathscr{W}_B - 1.7788780145 \times 10^{-2} = -3.8115.10^{-2}h^6$.

and the poloidal beta is unity. In eq. (6), E denotes the elongation, R_0 and a the major and the minor plasma radius, respectively. q_0 is the safety factor on the magnetic axis. The corresponding analytic formula for Ψ is

$$\Psi = \frac{E}{2R_0^3 q_0}\left(\frac{r^2 z^2}{E^2} + \tfrac{1}{4}\left(r^2 - R_0^2\right)^2 - a^2 R_0^2\right). \quad (7)$$

For the convergence study, we have chosen the Solovev equilibrium with $q_0 = \frac{3}{4}$, $E = 1$, $a = \frac{1}{3}$ and $R_0 = 1$.

In fig. 2, we observe that the poloidal magnetic field energy of the numerical solution converges towards its analytical value with an $\mathscr{O}(h^6)$ error.

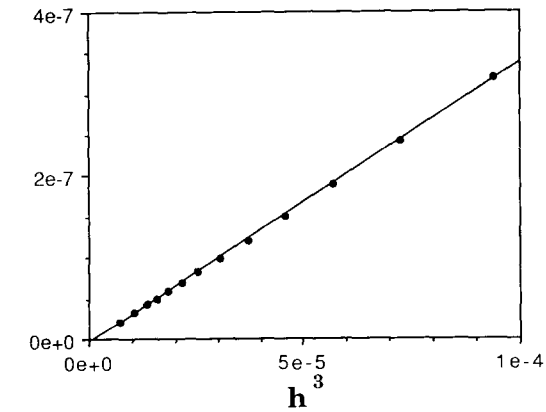

Fig. 3. Convergence of the magnetic axis of the Solovev test case. The regression curve is $R_m - 1 = 3.4184 \times 10^{-3}h^3$.

Figure 3 shows that the error in the magnetic axis R_m is $\mathscr{O}(h^3)$. Thus, the poloidal magnetic field energy and the magnetic axis converge according to theoretical expectation.

3.2. Non-linear equilibria

The Solovev equilibrium bypasses one difficulty in eq. (2): the problem loses its non-linearity, as the source term j_ϕ is independent of Ψ. We now consider a non-linear test case with geometry chosen to model JET (Joint European Torus). The plasma surface is defined by

$$\begin{aligned} r &= R_0 + a\cos(\theta + \delta \sin\theta), \\ z &= Ea \sin\theta, \end{aligned} \quad (8)$$

where a, E and R_0 have the same meaning as in eq. (6), and δ stands for the triangularity. For our test case, the inverse aspect ratio is $a/R_0 = 0.37$ and the other parameters are $E = 1.7$ and $\delta = 0.3$. We have chosen the following pressure and T^2 profiles:

$$\begin{aligned} p(\Psi/\Psi_{\min}) &= 0.07(\Psi/\Psi_{\min})^1, \\ T^2(\Psi/\Psi_{\min}) &= 0.983 + 0.1(\Psi/\Psi_{\min})^2 \\ &\quad - 0.083(\Psi/\Psi_{\min})^3. \end{aligned} \quad (9)$$

This equilibrium has been rescaled using the transformation described in appendix B such that the safety factor on the axis is $q_0 = 1.2$. Figure 4

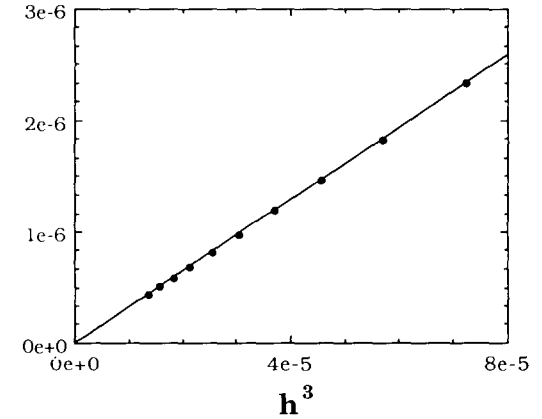

Fig. 4. Convergence of the magnetic axis of the JET test case. The regression curve is $R_m/R_0 - 1.05835305 = 3.231 \times 10^{-2}h^3$.

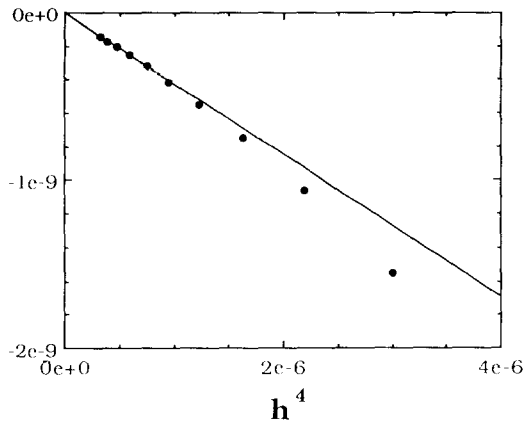

Fig. 5. Convergence of the poloidal magnetic energy of the JET test case. The full circle correspond to $\mathscr{W}_B - 6.0685373 \times 10^{-3}$. The equation of the solid line is $y = -4.2169 \times 10^{-4} h^4$.

shows that the magnetic axis converges according to theoretical prediction with an $\mathscr{O}(h^3)$ error. In the case where eq. (2) is a non-linear equation in Ψ, the poloidal magnetic field energy (5) no longer shows the $\mathscr{O}(h^6)$ convergence rate obtained for linear equilibria. Indeed, we observe in fig. 5 that the error in the poloidal magnetic field energy is asymptotically $\mathscr{O}(h^4)$ for the non-linear test case (9).

3.3. Discussion

The position of the magnetic axis is commonly used for validating equilibrium codes. In ref. [2] two Solovev cases were used as convergence tests of the finite linear "hybrid element" code CLIO, one with elongation $E = 1$, another with $E = 2$. For both test cases, $R_0 = 1$, $a = 0.4$ and $q_0 = 1$. According to the curves presented in ref. [2], the error in the magnetic axis is $R_m - 1 = 0.136h^2$ for the first case and $R_m - 1 = -0.130h^2$ for the second. We have computed the same equilibria with CHEASE. Linear regressions give $R_m - 1 = 9.2068 \times 10^{-3} h^3$ for the $E = 1$ case and $R_m - 1 = 9.9660 \times 10^{-3} h^3$ for the $E = 2$ case. Consequently, CLIO yields an error of $\Delta R_m \approx 1.5 \times 10^{-6}$ on the magnetic axis with a 300×300 mesh, whereas CHEASE needs only a 18×18 mesh to reach the same accuracy. The CPU time required for the calculation of these equilibria on the CRAY-2 is about 350 seconds for CLIO and 2.3 seconds for CHEASE.

The same comparison can be done with the JET test case shown in the same publication. There, the error in the magnetic axis behaves like $R_m/R_0 - 1.1014865 = -1.8193.10^{-2} h^3$ for CHEASE, and $R_m/R_0 - 1.1014865 = 0.1378h^2$ for CLIO. Therefore, CLIO gives an error of $\Delta R_m \approx 1.5 \times 10^{-6}$ in the magnetic axis with a 300×300 mesh, while CHEASE reaches a comparable precision on a 22×22 mesh. The resolution time on the CRAY-2 for this equilibrium is of 6.5 CPU seconds with CHEASE and of about 400 seconds with CLIO.

4. Mappings for ERATO and MARS

4.1. Computation of poloidal flux surface integrals

In this section, we discuss the mapping of the equilibrium into the flux coordinates and the calculation of the equilibrium quantities required by the two stability codes ERATO [9] and MARS [10]. ERATO is an ideal MHD stability code using the so-called "hybrid finite elements" in both the radial and poloidal directions. MARS is a resistive MHD stability code that uses Fourier decomposition in the poloidal angle and finite differences in the radial direction.

The flux coordinate system used by both stability codes differs completely from the one used for the equilibrium calculation. The radial stability coordinate of the two codes is

$$s = \sqrt{\frac{|\Psi_{\min} - \Psi|}{|\Psi_{\min}|}} . \tag{10}$$

The angular variable χ is defined by the choice of the Jacobian $J = [(\nabla\Psi \times \nabla\chi) \cdot \nabla\phi]^{-1}$ of the mapping from (Ψ, χ, ϕ)-space to Cartesian coordinates. In the equilibrium code, J is restricted to the form

$$J = C(\Psi) r^{\alpha} |\nabla\Psi|^{\mu}, \tag{11}$$

where α and μ are integers. $C(\Psi)$ is obtained by demanding that χ increases by 2π per poloidal turn.

The stability codes require equilibrium quantities of the form

$$\mathcal{F}(\Psi = \text{constant}, \chi) = \int_0^{\chi} f\left(\Psi, \frac{\partial\Psi}{\partial\sigma}, \frac{\partial\Psi}{\partial\theta}, \frac{\partial^2\Psi}{\partial\sigma\partial\theta}, \frac{\partial^2\Psi}{\partial\sigma^2}, \frac{\partial^2\Psi}{\partial\theta^2}\right) \times J \, d\chi'. \quad (12)$$

Most finite-element solutions of eq. (2) generate problems for an accurate computation of these kind of integrals. The Hermite cubic elements do not demand continuity on the cell edges for $\partial^2\Psi/\partial\sigma^2$ and $\partial^2\Psi/\partial\theta^2$. Thus, to perform integrals of the type of eq. (12) accurately, the integration interval is split into a set of subintervals delimited by the intersections of the constant-Ψ surfaces with the (σ, θ) cell edges. This allows the discontinuities which may appear in the integrand of eq. (12) to be avoided and a high-order integration scheme, such as Gaussian quadratures, can be applied.

4.2. Convergence studies of the mappings

The Solovev equilibrium described in section 3.1 allows one to avoid the solution of the Grad–Shafranov equation (2), because analytic values for Ψ, $\partial\Psi/\partial\sigma$, $\partial\Psi/\partial\theta$ and $\partial^2\Psi/\partial\sigma\partial\theta$ can be substituted on the nodes of the equilibrium mesh. Consequently, the mappings can be decoupled from the equilibrium solver in this case, and the convergence properties of the equilibrium quantities as well as the accuracy of the integration scheme presented in section 4.1 can be verified independently. The convergence properties of the mappings are checked by observing the growth rate (normalized to the Alfvén frequency) of the most unstable linear eigenmode. For this test, we keep the stability meshes fixed and increase the equilibrium mesh density. For the three test cases, the χ-coordinate defined by the constant volume Jacobian ($J = C(\Psi)$ or $\alpha = 0$ and $\mu = 0$ in eq. (11)) gives good results for the stability calculations (better than with straight field lines). The s-mesh has been packed on all resonant-q surfaces.

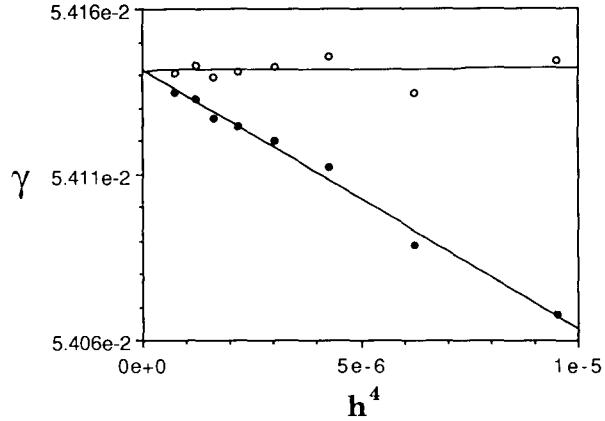

Fig. 6. Convergence of the growth rate of the Solovev test case with ERATO.

The equilibrium quantities employed for the stability calculation are given in appendix C. They depend on Ψ, $\nabla\Psi$ and second derivatives of Ψ. We are not aware of a theoretical prediction for the convergence of the stability eigenvalues with the equilibrium mesh.

For the Solovev test case, we have computed the growth rate for toroidal mode number $n = 3$, with a perfectly conducting wall on the plasma edge. The stability mesh is fixed to $N_s = 100$ radial and $N_\chi = 100$ intervals with ERATO, and $N_s = 110$ radial points and $N_m = 11$ Fourier components in the χ-direction with MARS. The error in the growth rate obtained with the analytic solution on the equilibrium gridpoints (full circles

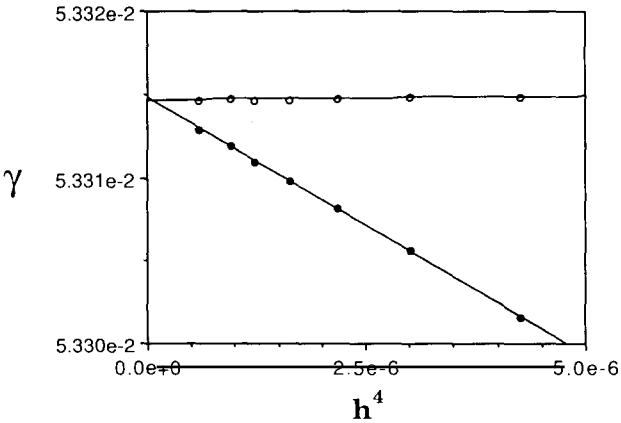

Fig. 7. Convergence of the growth rate of the Solovev test case with MARS.

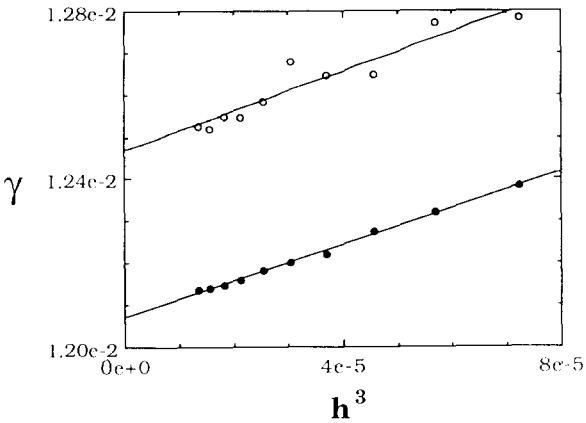

Fig. 8. Convergences of growth rates of the JET test case with ERATO (open circles) and MARS (full circles).

in figs. 6 and 7) converges as $\mathcal{O}(h^4)$ with some oscillations superposed for ERATO. It appears that the dominant error in the growth rate comes from the $\mathcal{O}(h^4)$ convergence of Ψ when the analytic solution is injected on the nodes. A check on the convergence of the poloidal magnetic field energy reveals a $\mathcal{O}(h^4)$-behaviour in this case, instead of $\mathcal{O}(h^6)$ for the numerical solution. With the numerical solution (open circles, figs. 6 and 7), the $\mathcal{O}(h^4)$-error in the growth rate appearing with the analytical solution is removed for both stability codes and only the oscillatory behaviour remains, probably because the finite-element representation minimizes errors in a global sense. However, the error in the growth rate is much smaller than with the analytic solution on the equilibrium gridpoints.

The JET case described in section 3.2 shows a $n = 1$ instability with a perfectly conducting wall placed at one minor radius from the plasma surface. In fig. 8, we observe that the growth rate converges as $\mathcal{O}(h^3)$ with the two stability codes. The open circles are obtained with ERATO, and the full circle with MARS. Here, the fixed stability meshes are $N_s = 180$ radial and $N_\chi = 180$ intervals with ERATO, and the same as for the Solovev case with MARS.

4.3. Discussion

The values of the growth rates after convergence of the equilibrium are slightly different with ERATO and MARS because the discretization methods used in the two stability codes lead to different truncation errors. After convergence of the stability calculations with fixed equilibrium mesh ($N_{\sigma r} = N_\theta = 40$), both codes give the same growth rates: $\gamma = 5.395 \times 10^{-2}$ for the Solovev and $\gamma = 1.231 \times 10^{-2}$ for the JET test case. It should be noted that 10^{-2} is a typical growth rate for production runs in the context of beta-limit studies.

It is interesting to compare the results of section 4.2 with those obtained by other codes. Although convergence properties of many equilibrium codes are available in the literature, to our knowledge no convergence curves have been published showing the error due to the equilibrium calculation on the stability results.

We have used the equilibrium code EQLAUS [5] combined with ERATO for such a comparison with CHEASE. EQLAUS uses a finite-difference scheme in Cartesian coordinates for the discretization. We have reproduced the non-linear JET case shown in section 3 with this numerical package. The ERATO mesh has been fixed ($N_s = N_\chi = 180$), and the same radial stability mesh packing was used than with CHEASE.

For this test case, the growth rate behaves like $\gamma = 1.247 \times 10^{-2} - 0.461h$ with EQLAUS + ERATO, $\gamma = 1.247 \times 10^{-2} + 4.691h^3$ with CHEASE + ERATO and $\gamma = 1.2070 \times 10^{-2} + 4.316h^3$ with CHEASE + MARS (see fig. 8). Thus, the error in the growth rate due to EQLAUS is of about $\Delta\gamma = 1.5 \times 10^{-3}$ on a 300×300 mesh. This precision is already reached on a 16×16 mesh with CHEASE and ERATO. On the CRAY-2, the computation of a 300×300 case with EQLAUS takes about 300 CPU seconds, while a 16×16 case with CHEASE requires only about 15 seconds, including in both cases the computation of the stability input quantities, ballooning and local stability criteria (see appendix C).

5. Implementation

Figure 9 shows the CPU time needed to calculate a non-linear test case and the quantities

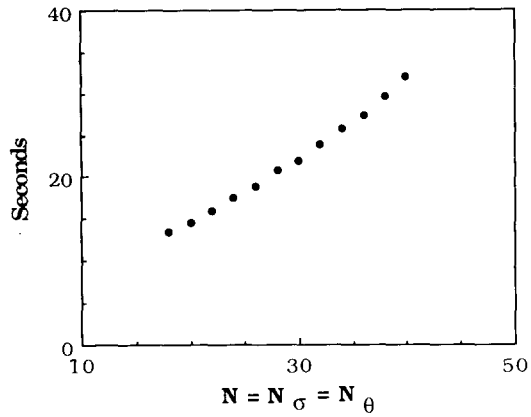

Fig. 9. Computation time on the CRAY-2 for non-linear equilibria including mapping to flux coordinates, ballooning and local stability criterions.

required by the stability codes on the CRAY-2. The most time-consuming operations are the Gauss elimination used in the solution of eq. (2), and the tracing of constant flux surfaces. The first operation is well vectorized, the second would be easy to parallelize: each constant poloidal flux surface can be traced by a different processor of the computer. However, this option has not yet been implemented.

The equilibrium solver needs approximatively $4N_\theta N_\sigma(4N_\theta + 300)$ Mwords of central memory storage space, the mapping for MARS $120N_sN_\theta + 50N_sN_m$ Mwords, where N_m is the number of poloidal modes for the Fourier decomposition, and the mapping for ERATO $120N_sN_\theta + 40N_\chi N_s$ Mwords. The code has now been implemented on different types of computers (CRAY, IBM, SUN), and is easily transportable.

6. Conclusion

The Hermite bicubic elements have proved their efficiency in the solution of the Grad–Schlüter–Shafranov equation. The convergence rates of the equilibrium solution agree with the theoretical predictions, despite the special treatment on the axis of the modified polar mesh used for the discretization. Moreover, the results presented in sections 3 and 4 indicate that the slopes of the convergence curves are very small. This has been confirmed by extensive use of the code.

To study the effect of the equilibrium calculation and the mapping to flux coordinates on the accuracy of the stability calculations, we have shown convergence tests with the stability codes ERATO using two-dimensional linear "hybrid elements", and MARS, where Fourier decomposition is used in the poloidal direction. For both codes, the error due to the equilibrium solver on the stability results converges in $\mathcal{O}(h^3)$, to be compared with the $\mathcal{O}(h)$-error if second-order accurate finite differences are used for the discretization of the equilibrium.

Acknowledgements

This work was supported in part by the Swiss National Science Foundation.

Appendix A. Solution of the Grad–Shafranov equation

In the standard manner of the finite-element method, eq. (2) is solved in the coordinate system (4) by expanding Ψ in Hermite bicubics on a rectangular grid in σ and θ. The equation is then multiplied by an arbitrary weighting function from the same function space as Ψ and is integrated in space. The integrals are carried out numerically using a Gaussian quadrature formula.

The Hermite bicubics use as unknowns the values of the function Ψ, its first derivatives $\partial\Psi/\partial\sigma$ and $\partial\Psi/\partial\theta$ and the mixed second derivative $\partial^2\Psi/\partial\sigma\partial\theta$, all on the nodes of the mesh. The boundary condition $\Psi \equiv 0$ on $\delta\Omega$ implies $\Psi = 0$ and $\partial\Psi/\partial\theta = 0$ for all the boundary points $\sigma = 1$ and $\theta = \theta_j$, $j = 1, \ldots, N_\theta$, where N_θ is the number of intervals in the θ-direction. The origin of the polar coordinate system requires some extra care as the coordinate transformation (4) becomes singular there and one single geometrical point is represented by N_θ mesh points. We impose the condition that Ψ must be a regular function of r and z at the origin. A first-order Taylor expan-

sion of Ψ around (r_0, z_0), when expressed in terms of (σ, θ)leads to

$$\Psi = \Psi_c + \sigma\rho_s(\theta)[\Psi_r \cos\theta + \Psi_z \sin\theta] + \mathcal{O}(\sigma^2). \quad (13)$$

Thus, the regularity condition forces the $4N_\theta$ unknowns Ψ, $\partial\Psi/\partial\sigma$, $\partial\Psi/\partial\theta$ and $\partial^2\Psi/\partial\sigma\partial\theta$ for $\sigma = 0$ and $\theta = \theta_j$, $j = 1, \ldots, N_\theta$ to be replaced by the three unknowns Ψ_c, Ψ_r and Ψ_z. We impose the following conditions by collocation on the N_θ grid points for $\sigma = 0$:

$$\begin{aligned}
&\Psi = \Psi_c,\\
&\frac{\partial\Psi}{\partial\theta} = 0,\\
&\frac{\partial\Psi}{\partial\sigma} = \rho_s(\theta)[\Psi_r \cos\theta + \Psi_z \sin\theta], \quad (14)\\
&\frac{\partial^2\Psi}{\partial\sigma\partial\theta} = \rho_s(\theta)[-\Psi_r \sin\theta + \Psi_z \cos\theta]\\
&\qquad + \frac{\mathrm{d}\rho_s}{\mathrm{d}\theta}[\Psi_r \cos\theta + \Psi_z \sin\theta].
\end{aligned}$$

The functions p and T^2 that define the toroidal current density are functions of $\Psi/\Psi_{\min}$ (Ψ is negative inside the plasma). Equation (2) is then solved iteratively by a Picard method

$$\nabla\cdot\frac{1}{r^2}\nabla\Psi_{k+1} = -\frac{\mathrm{d}p_k}{\mathrm{d}\Psi} - \frac{1}{2r^2}\frac{\mathrm{d}T_k^2}{\mathrm{d}\Psi} = \frac{j_{\phi k}}{r}. \quad (15)$$

The iteration is terminated when

$$\frac{\| \Psi_{k+1} - \Psi_k \|}{\| \Psi_k \|} < \epsilon, \quad (16)$$

where ϵ is a predefined number. The norm used in eq. (16) is $\| u \| = [(\Sigma_{\text{nodes}} u^2)/N_{\text{nodes}}]^{1/2}$.

The iterations are normally done first on a coarse grid ($N_\sigma \times N_\theta = 16 \times 16$) and later on a more refined grid. For the coarse grid, the centre of the polar coordinates is chosen as the geometrical midpoint of the plasma. For the refined grid, we choose the magnetic axis of the approximate solution as the centre of the polar coordinates. This is done to facilitate the subsequent mapping to flux coordinates (see section 4).

Appendix B. Transformation of the equilibrium

It is well known [9] that a single solution of the Grad–Shafranov equation can be used to generate a whole sequence of equilibria with fixed poloidal beta but different plasma current and rotational transform. Two transformations which leave eq. (2) unchanged are used to effect this. The first is a scaling:

$$\Psi_{\text{new}} = \mu\Psi_{\text{old}},\ T_{\text{new}} = \mu T_{\text{old}},\ p_{\text{new}} = \mu^2 p_{\text{old}}. \quad (17)$$

The second shift of T^2:

$$T^2_{\text{new}} = T^2_{\text{old}} + C, \quad (18)$$

leaving Ψ and p unchanged. These transformations are used in CHEASE to generate equilibria with prescribed values of either the total current (3) or of the safety factor

$$q(\Psi_q) = \frac{T(\Psi_q)}{2\pi}\oint_{\Psi_q = \text{constant}} \frac{\mathrm{d}l}{r\,|\nabla\Psi|} \quad (19)$$

on some arbitrary flux surface Ψ_q. The existence of two transformations also allows specification of T on a given flux surface Ψ_T.

When the total current is specified, we first rescale using eq. (17) with $\mu = I_{\text{specified}}/I_{\text{old}}$ and then shift using eq. (18) with $C = T^2_{\text{specified}}(\Psi_T) - T^2(\Psi_T)$, where T denotes the value after rescaling. When the safety factor is prescribed, we first shift T^2 by $C = [q^2_{\text{specified}}/q^2_{\text{old}}(\Psi_q) - 1]T^2(\Psi_q)$ and then rescale the solution by $\mu = T_{\text{specified}}/T(\Psi_T)$, where T denotes the value after the shift.

After the transformation of the equilibrium, all relevant physical quantities characterising the equilibrium can be computed. A list of these quantities is shown in table 1.

Appendix C. Input quantities for linear-stability codes

The non-orthogonality of the stability mesh

$$\beta_{\Psi\chi} = \frac{\nabla\Psi\cdot\nabla\chi}{|\nabla\Psi|^2} \quad (20)$$

Table 1
Physical quantities computed by equilibrium code

Global quantities	
Total plasma volume/2π	$V_{\rm tot} = \int_\Omega J \, \mathrm{d}\Psi \mathrm{d}\chi$
Volume average	$\bar{f} = (\int_\Omega fJ \, \mathrm{d}\Psi \mathrm{d}\chi)/V_{\rm tot}$
Total toroidal current	$I_\phi = \int_\Omega j_\phi (J/r) \, \mathrm{d}\Psi \mathrm{d}\chi$
Plasma inductance	$l_i = \dfrac{4\pi}{I_\phi^2 R_{\rm mag}} \int_\Omega \dfrac{\lvert\nabla\Psi\rvert^2}{r^2} J \, \mathrm{d}\Psi \mathrm{d}\chi$
Total beta	$\beta = \dfrac{2\bar{p}}{\overline{B^2}}$
Fusion beta	$\beta^* = \dfrac{2(\overline{p^2})^{1/2}}{\overline{B^2}}$
Poloidal beta	$\beta_p = \dfrac{8\pi}{I_\phi^2 R_{\rm mag}} \bar{p} V_{\rm tot}$
Flux surface quantities	
Volume of Ψ = const/2π	$V(\Psi) = \int_{\Psi' = \Psi_{\min}}^{\Psi} \oint J \, \mathrm{d}\chi \mathrm{d}\Psi'$
Generalized radius of Ψ = constant	$\rho(\Psi) = (V(\Psi)/V_{\rm tot})^{1/2}$
Toroidal current within Ψ = constant	$I_\phi(\Psi) = \int_{\Psi' = \Psi_{\min}}^{\Psi} \oint j_\phi (J/r) \, \mathrm{d}\chi \mathrm{d}\Psi'$
Poloidal beta on Ψ = constant	$\beta_p(\Psi) = -\dfrac{8\pi}{I_\phi^2(\Psi) R_{\rm mag}} \int_{\Psi' = \Psi_{\min}}^{\Psi} p'(\Psi') V(\Psi') \, \mathrm{d}\Psi'$
Global shear on Ψ = constant	$\hat{s}(\Psi) = \dfrac{\rho}{q(\Psi)} \dfrac{dq}{d\rho}(\Psi)$
Local quantities	
Local shear	$\hat{s}_{\rm local} = -\dfrac{(\boldsymbol{B} \times \nabla\Psi)}{\lvert\nabla\Psi\rvert^2} \cdot \nabla \times \dfrac{(\boldsymbol{B} \times \nabla\Psi)}{\lvert\nabla\Psi\rvert^2}$
Magnetic field-line curvature	$\kappa = \dfrac{1}{B^2} \nabla\Psi \cdot (\boldsymbol{B} \cdot \nabla)\boldsymbol{B}$

is obtained by integrating

$$\mathrm{d}\beta_{\Psi\chi} = \left(\frac{r j_\phi}{\lvert\nabla\Psi\rvert^2} + (2-\alpha) \left[\frac{\partial(\ln r)}{\partial\Psi} \right]_n - (\mu+2) \left[\frac{\partial(\ln \lvert\nabla\Psi\rvert)}{\partial\Psi} \right]_n - \frac{C'(\Psi)}{C(\Psi)} \right) \mathrm{d}\chi, \tag{21}$$

with respect to χ. The index n in eq. (21) stands for the normal derivative with respect to Ψ, j_ϕ is defined by eq. (2) and $C'(\Psi)$ is derived from the periodicity condition $\beta_{\Psi\chi}(0) = \beta_{\Psi\chi}(2\pi)$.

The stability codes use an "integer mesh", with rather arbitrarily defined χ_k such that $0 = \chi_1 < \ldots < \chi_{N_\chi} + 1 = 2\pi$, and a "half mesh" $\chi_{k+1/2} = (\chi_k + \chi_{k+1})/2$ for $k = 1, \ldots, N_\chi$. Similar integer and half meshes are used in the s-direction.

C.1. ERATO

For ERATO, all quantities of the equilibrium involved in the stability calculation must be computed at the centres of the stability mesh cells. In table 2 all quantities with $j > 6$ are computed on the $(s_{l+1/2}, \chi_{k+1/2})$-mesh, except at the plasma edge. This is stored into an array EQ(j; k; l), for $k = 1, \ldots, N_\chi$ and $l = 1, \ldots, N_s + 1$.

C.2. MARS

MARS uses finite differences in the radial and Fourier decomposition in the poloidal and toroidal directions. All equilibrium quantities

Table 2
Input quantities for ERATO

j	EQ(j; k; l)
1	s_l
2	χ_k
3	s_{l+1} for $l \neq N_s+1$ and s_{l-1} is free for $l = N_s+1$
4	χ_{k+1}
5	$s_{l+1/2} = (s_l + s_{l+1})/2$ for $l \neq N_s+1$ and $s_{l+1/2} = 1$ for $l = N_s+1$
6	$\chi_{k+1/2} = (\chi_k + \chi_{k+1})/2$
7	mass density ρ
8	plasma pressure $\gamma p / q_0 \lvert \Psi_{\min} \rvert$
9	toroidal magnetic flux T
10	free
11	q/q_0
12	poloidal magnetic field $\Psi r^2 / q_0 \lvert \nabla\Psi \rvert^2$
13	non-orthogonality $\beta_{s\chi} = 2s \lvert \Psi_{\min} \rvert \beta_{\Psi\chi}$
14	r^2
15	$\left[\frac{\partial \ln r^2}{\partial s}\right]_\chi$
16	$\left[\frac{\partial \ln r^2}{\partial \chi}\right]_s$
17	$H = -2s \lvert \Psi_{\min} \rvert \left(\frac{r j_\phi}{\lvert \nabla\Psi \rvert^2} - \left[\frac{\partial \ln(r^2/J)}{\partial \Psi}\right]_\chi \right)$
18	$K = \frac{2\Psi}{q_0}\left(\frac{j_\phi^2}{\lvert \nabla\Psi \rvert^2} - \frac{j_\phi}{r}\left[\frac{\partial \ln \lvert \nabla\Psi \rvert}{\partial \Psi}\right]_n - p'\left[\frac{\partial \ln r}{\partial \Psi}\right]_n \right)$
19	r^2/J
20	$\left[\frac{\partial \ln(r^2/J)}{\partial \chi}\right]_\Psi$
21	$\frac{\partial}{\partial s}\left[\int_0^\chi \frac{JT}{r^2}\, \mathrm{d}\chi'\right]_\chi$
22	non-orthogonality $\beta_{s\chi}^{\mathrm{S.F.}} = 2s \lvert \Psi_{\min} \rvert \beta_{\Psi\chi}^{\mathrm{S.F.}}$ with straight field lines
23	$\left[\frac{\partial \lvert \nabla\Psi \rvert^2}{\partial \chi}\right]_\Psi$

necessary for MARS are directly Fourier transformed in the mapping. For this operation, we apply the integration method described in section 4.1 to

$$f(m, n=0) = \frac{1}{2\pi}\oint_{\Psi=\text{constant}} f\, \mathrm{e}^{im\chi}\, \mathrm{d}\chi, \qquad (22)$$

where f represents any EQL in table 3. MARS requires these quantities both on the half and the integer mesh. All quantities in table 3 are expressed as function of the Jacobian

Table 3
Input quantities for MARS

j	EQL(j)
1	$\frac{g_{ss}}{J_s} = J_s\left(\beta_{s\chi}\frac{\lvert \nabla s \rvert}{r}\right)^2 + \frac{1}{J_s \lvert \nabla s \rvert^2}$
2	$\frac{g_{\chi\chi}}{J_s} = J_s\left(\frac{\lvert \nabla s \rvert}{r}\right)^2$
3	$\frac{g_{\phi\phi}}{J_s} = \frac{r^2}{J_s}$
4	$\frac{g_{s\chi}}{J_s} = -J_s\beta_{s\chi}\left(\frac{\lvert \nabla s \rvert}{r}\right)^2$
5	$J_s g_{ss}$
6	$J_s g_{\chi\chi}$
7	$J_s g_{\phi\phi}$
8	$J_s g_{s\chi}$
9	J_s
10	$J_s j^\chi = -2s \lvert \Psi_{\min} \rvert T'(\Psi)$
11	$J_s j^\phi = -J_s[p'(\Psi) + T(\Psi)T'(\Psi)/r^2]$
12	$J_s B^\chi = 2s \lvert \Psi_{\min} \rvert$
13	$J_s B^\phi = J_s T(\Psi)/r^2$
14	$p(\Psi)$
15	$\frac{\mathrm{d}p}{\mathrm{d}s} = 2s \lvert \Psi_{\min} \rvert p'(\Psi)$

$$J_s = \left[(\nabla s \times \nabla\chi)\cdot\nabla\phi\right]^{-1} = 2s \lvert \Psi_{\min} \rvert J \qquad (23)$$

and

$$\beta_{s\chi} = \frac{\nabla s \cdot \nabla\chi}{\lvert \nabla s \rvert^2} = 2s \lvert \Psi_{\min} \rvert \beta_{\Psi\chi}, \qquad (24)$$

where J is given by eq. (11) and $\beta_{\Psi\chi}$ by eq. (20).

C.3. Ballooning stability, Mercier and resistive interchange criterion

Ballooning modes are toroidal modes with infinite toroidal mode number n [17,18]. The potential energy for these modes is given by

$$\delta W_{\mathrm{p}}(n\to\infty) = \frac{1}{2}\int_{-\infty}^{+\infty}\left\{ f\left\lvert \frac{\partial \xi}{\partial \chi}\right\rvert^2 + g \lvert \xi \rvert^2 \right\} J\, \mathrm{d}\chi, \qquad (25)$$

where ξ is the radial component of the displacement vector, and χ is a generalized poloidal angle extending from $-\infty$ to $+\infty$. For ballooning stability, δW_{p} must be positive definite on every

flux surface. The quantities appearing in eq. (25) are [17]:

$$
\begin{aligned}
\nu &= \frac{JT}{r^2}, \\
B^2 &= \frac{1}{r^2}\left[T^2 + |\nabla\Psi|^2\right], \\
f &= \frac{1}{J^2|\nabla\Psi|^2}\left(1 + \frac{|\nabla\Psi|^4}{B^2}G^2\right), \\
g &= -\frac{2p'}{B^2}\left[\left(\frac{\partial\tilde{P}}{\partial\Psi}\right)_n - \frac{TG}{B^2}\frac{1}{J}\left(\frac{\partial\tilde{P}}{\partial\chi}\right)_\Psi\right], \\
G &= \nu\beta_{\Psi\chi} + \int_{\chi_0}^{\chi}\left(\frac{\partial\nu}{\partial\Psi}\right)_\chi \mathrm{d}\chi', \\
\tilde{P} &= p + \tfrac{1}{2}B^2.
\end{aligned}
\tag{26}
$$

The integral (25) is solved on the (Ψ, χ)-mesh of ERATO by a hybrid linear finite-element method. The infinite χ-integration interval of eq. (25) is replaced by a finite one specified as input (normally $20 \times 2\pi$) outside which ξ is set to zero. For the arbitrary angle χ_0, 25 different values are tested on every constant-Ψ surface. The diagonalization of the matrix corresponding to the variation of problem (25) is not unique, but according to Sylvester's theorem [19], the number of negative terms in the diagonal matrix is invariant and equal to the number of unstable ballooning modes on the particular poloidal flux surface.

The Mercier stability [20] and the resistive interchange criterion [21] are checked on every constant poloidal flux surface. Let us define the integrals

$$
\begin{aligned}
J_1 &= \frac{1}{2\pi}\oint_{\Psi=\text{constant}} \frac{1}{r^2|\nabla\Psi|^2} J\,\mathrm{d}\chi, \\
J_2 &= \frac{1}{2\pi}\oint_{\Psi=\text{constant}} \frac{1}{|\nabla\Psi|^2} J\,\mathrm{d}\chi, \\
J_3 &= \frac{1}{2\pi}\oint_{\Psi=\text{constant}} \frac{r^2}{|\nabla\Psi|^2} J\,\mathrm{d}\chi, \\
J_4 &= \frac{1}{2\pi}\oint_{\Psi=\text{constant}} \frac{1}{r^2} J\,\mathrm{d}\chi, \\
J_5 &= \frac{1}{2\pi}\oint_{\Psi=\text{constant}} J\,\mathrm{d}\chi, \\
J_6 &= \frac{1}{2\pi}\oint_{\Psi=\text{constant}} \frac{|\nabla\Psi|^2}{r^2} J\,\mathrm{d}\chi.
\end{aligned}
\tag{27}
$$

A given flux surface is stable to ideal interchanges if the Mercier criterion $-D_I > 0$, where

$$
-D_I = \left(\frac{p'TJ_2}{q'} - \frac{1}{2}\right)^2 + \frac{p'}{q'^2}\left(J_5' - p'J_3\right)\left(T^2J_1 + J_4\right). \tag{28}
$$

Resistive interchanges are stable if $-D_R > 0$ with

$$
-D_R = -D_I - \left(H - \tfrac{1}{2}\right)^2 \tag{29}
$$

and

$$
H = \frac{Tp'}{q'}\left(J_2 - \frac{J_5\left(J_4 + T^2J_1\right)}{J_6 + T^2J_4}\right). \tag{30}
$$

The prime in eqs. (28) and (30) denotes the derivative with respect to Ψ.

References

[1] J. Blum, J. Le Foll and B. Thooris, Comput. Phys. Commun. 24 (1981) 235.
[2] R. Gruber, R. Iacono and F. Troyon, J. Comput. Phys. 73 (1987) 168.
[3] J.L. Johnson et al., J. Comput. Phys. 32 (1979) 212.
[4] J. DeLucia, S.C. Jardin and A.M.M. Todd, J. Comput. Phys. 37 (1980) 183.
[5] A.D. Turnbull, M.A. Secrétan, F. Troyon, S. Semenzato and R. Gruber, J. Comput. Phys. 66 (1986) 391.
[6] K.M. Ling and S.C. Jardin, J. Comput. Phys. 58 (1985) 300.
[7] L.L. Lao, S.P. Hirshman and R.M. Wieland, Phys. Fluids 24 (1981) 1431.
[8] L.L. Lao, Comput. Phys. Commun. 31 (1984) 201.
[9] R. Gruber et al., Comput. Phys. Commun. 21 (1981) 323.
[10] A. Bondeson, G. Vlad and H. Lütjens, in: Controlled Fusion and Plasma Physics, Proc. 17th European Conf., Amsterdam, 1990 (European Phys. Soc., Geneva, 1990), part II, p. 906.
[11] J.M. Greene and J.L. Johnson, Phys. Fluids 5 (1962) 510.
[12] V.D. Shafranov, Sov. Phys. JETP 8 (1958) 494; Zh. Eksp. Teor. Fiz. 33 (1957) 710.
[13] R. Lüst and A. Schlüter, Z. Naturforsch. 129 (1957) 850.
[14] H. Grad and H. Rubin, in: Proc. Second Int. Conf. on the Peaceful Uses of Atomic Energy (United Nations, Geneva, 1958), vol. 31, p. 190.
[15] G. Strang and G. Fix, An Analysis of the Finite Element Method (Prentice-Hall, Englewood Cliffs, NJ, 1973).
[16] L.S. Solovev, Sov. Phys. JETP 26 (1968) 400; Zh. Eksp. Fiz. 53 (1967) 626.
[17] J.W. Connor, R.J. Hastie and J.B. Taylor, Phys. Rev. Lett. 40 (1978) 396.

[18] D. Dobrott, D.B. Nelson, J.M. Greene, A.H. Glasser, M.S. Chance and E.A. Frieman, Phys. Rev. Lett. 39 (1977) 943.
[19] W. Graeub, Die Grundlehren der mathematischen Wissenschaften, Band XCVII, Lineare Algebra (Springer Berlin, 1958) p. 157.
[20] C. Mercier, Nucl. Fusion Suppl. 2 (1962) 801.
[21] A.H. Glasser, J.M. Greene and J.L. Johnson, Phys. Fluids 18 (1975) 875.